The Astrophysical Journal, 607:778–787, 2004 June 1

HIGH-ENERGY GAMMA-RAY OBSERVATIONS OF W COMAE WITH THE SOLAR TOWER ATMOSPHERIC CERENKOV EFFECT EXPERIMENT (STACEE)

R. A. Scalzo,[1,2] L. M. Boone,[3,4] D. Bramel,[5] J. Carson,[6] C. E. Covault,[7] P. Fortin,[8] G. Gauthier,[8] D. M. Gingrich,[9,10] D. Hanna,[8] A. Jarvis,[6] J. Kildea,[8] T. Lindner,[8] C. Mueller,[8] R. Mukherjee,[5] R. A. Ong,[6] K. J. Ragan,[8] D. A. Williams,[3] and J. Zweerink[6]
(The STACEE Collaboration)
Received 2003 December 12; accepted 2004 February 11

ABSTRACT

We report on observations of the blazar W Com (ON+231) with the Solar Tower Atmospheric Cerenkov Effect Experiment (STACEE), a wave front–sampling atmospheric Cerenkov telescope, in the spring of 2003. In a data set comprising 10.5 hr of on-source observing time, we detect no significant emission from W Com. We discuss the implications of our results in the context of the composition of the relativistic jet in W Com, examining both leptonic and hadronic models for the jet. We derive 95% confidence level upper limits on the flux at the level of (1.5–3.5) $\times 10^{-10}$ cm^{-2} s^{-1} above 100 GeV for the leptonic models, or (0.5–1.1) $\times 10^{-10}$ cm^{-2} s^{-1} above 150 GeV for the hadronic models.

Subject headings: BL Lacertae objects: individual (W Com) — galaxies: active — gamma rays: observations

1. INTRODUCTION

The current catalog of extragalactic TeV gamma-ray sources consists of blazars, which are among the brightest and most rapidly variable objects in the sky. The unusual observational properties of blazars are usually explained in terms of relativistic bulk motion of the emitting region in a jet parallel to the line of sight (Urry & Padovani 1995). The continuum emission of blazars is typically nonthermal and contains two broad peaks, one at lower energies (radio to X-ray) and one at higher energies (keV to TeV). Although the low-energy peak is generally assumed to result from synchrotron radiation from high-energy electrons in the jet, the mechanism for the production of the high-energy radiation is still a subject of debate, and several competing models exist.

In "leptonic" jet models, the high-energy radiation is produced by inverse Compton scattering of low-energy photons from a population of electrons and/or positrons; these models are favored for the well-studied blazars Mrk 421 and 501 (Coppi & Aharonian 1999; Konopelko et al. 2003). In the synchrotron self-Compton model (SSC), a single population of electrons and positrons produce the target photon field via synchrotron radiation and subsequently upscatter the synchrotron photons to gamma-ray energies (Bloom & Marscher 1996). There may also be an external Compton (EC) component of target photons from the accretion disk or ambient medium (Dermer et al. 1992; Sikora et al. 1994). Alternatively, in "hadronic" jet models, protons play a central role. In hadronic models the high-energy radiation is attributed to photomeson processes (Mannheim 1993) or synchrotron radiation from protons or muons, as in the synchrotron proton blazar (SPB) model (Mücke & Protheroe 2000; Aharonian 2000; Mücke et al. 2003). The study of hadronic models was originally motivated by the hypothesis that the highest energy cosmic rays are produced in blazar jets (Mannheim 1995).

The BL Lac object W Com (ON+231) may provide an excellent test case for hadronic jet models (Boettcher et al. 2002). The transition between the low-energy and high-energy peaks in the continuum of W Com appears clearly in X-ray data taken by the *BeppoSAX* satellite (Tagliaferri et al. 2000). These high-quality observations of the transition region place tight constraints on leptonic models, requiring the predicted gamma-ray emission to cut off sharply above 100 GeV. In contrast, hadronic models may allow for significant emission above 100 GeV. Observations by the EGRET detector on board the *Compton Gamma Ray Observatory* show a hard power-law spectrum (photon spectral index $\alpha = 1.73 \pm 0.18$) extending up to about 10 GeV with no sign of any cutoff (Hartman et al. 1999). However, the object has not been detected at energies above 300 GeV, despite repeated observation by the Whipple 10 m instrument (Horan et al. 2003). At a redshift of 0.1, absorption of gamma rays in this energy range by pair production $\gamma\gamma \longrightarrow e^+e^-$ against the extragalactic background light (EBL) may be significant, but only at energies above about 500 GeV (Primack et al. 1999, 2001; Malkan & Stecker 2001; Aharonian 2001), so the intrinsic emission spectrum of W Com should be directly observable at energies lower than this.

The Solar Tower Atmospheric Cerenkov Effect Experiment (STACEE) currently operates above an energy threshold of about 100 GeV for gamma rays. W Com has been observed in the past with previous versions of the STACEE detector (Théoret 2001). New observations of W Com were carried out

[1] Enrico Fermi Institute, University of Chicago, 5640 South Ellis Avenue, Chicago, IL 60637.
[2] Current address: Lawrence Berkeley National Laboratory, MS 50R5008, 1 Cyclotron Road, Berkeley, CA 94720.
[3] Santa Cruz Institute for Particle Physics, University of California at Santa Cruz, 1156 High Street, Santa Cruz, CA 95064.
[4] Current address: Department of Physics, College of Wooster, Wooster, OH 44691.
[5] Department of Physics and Astronomy, Barnard College and Columbia University, New York, NY 10027.
[6] Department of Physics and Astronomy, University of California at Los Angeles, Box 951547, Knudsen Hall, Los Angeles, CA 90095-1547.
[7] Department of Physics, Case Western Reserve University, 10900 Euclid Avenue, Cleveland, OH 44106.
[8] Department of Physics, McGill University, 3600 University Street, Montreal, QC H3A 2T8, Canada.
[9] Centre for Subatomic Research, University of Alberta, Edmonton, AB T6G 2N5, Canada.
[10] Tri-Universities Meson Facility, Vancouver, BC V6T 2A3, Canada.

in the spring of 2003 by the most recent version of the detector, STACEE-64.

2. THE STACEE DETECTOR

STACEE is an atmospheric Cerenkov telescope that uses as its primary optic an array of solar mirrors (heliostats) at the National Solar Thermal Test Facility (NSTTF) in Albuquerque, NM. STACEE uses the independently steerable heliostats to collect Cerenkov light from extensive air showers initiated by astrophysical gamma rays. Secondary mirrors are used to image the heliostat field onto a camera of photomultiplier tubes (PMTs), producing a one-to-one mapping between heliostats and PMTs. Optical concentrators based on the DTIRC design (Ning et al. 1987) widen the aperture of each PMT from 5 to 11 cm and restrict its field of view to reduce the number of night-sky background (NSB) photons detected. High-speed electronics measure the charge and relative arrival times of the PMT pulses and impose a coincidence trigger. The STACEE detector is thus a *wave front–sampling* detector, measuring the intensity and arrival time of the narrow wave front of Cerenkov light at different spots on the ground. These measurements enable the off-line reconstruction of the primary energy and shower arrival direction.

STACEE achieves a low-energy threshold ($\sim$100 GeV) for the detection of gamma rays (compared with contemporary single-dish imaging Cerenkov telescopes) primarily because of the extremely large available mirror area ($A \sim 10^3$ m^2); the energy threshold scales approximately as $A^{-1/2}$ (Weekes 1988). Other instruments using a similar solar tower design include the Cerenkov Low Energy Sampling and Timing Experiment (CELESTE) in Themis, France (de Naurois et al. 2002) and the Solar Two detector in Barstow, CA (Tripathi et al. 2002). These are the only experiments currently operating in the Northern Hemisphere that have their peak sensitivity to gamma rays below 300 GeV.

STACEE has undergone a series of upgrades and improvements over its lifetime. The prototype experiment, called STACEE-32, used 32 heliostats with a total mirror area of 1200 m^2 (Hanna et al. 2002) and successfully detected gamma-ray emission from the Crab Nebula at a peak energy of 190 GeV (Oser et al. 2001). An upgraded detector called STACEE-48 used an additional 16 heliostats (for a total of 48) and employed improved high-speed programmable delay and trigger electronics (Martin & Ragan 2000); it detected gamma-ray emission from Mrk 421 during a period of intense flaring activity (Boone et al. 2002), as part of a multiwavelength variability study. The final stage of construction, called STACEE-64, was completed in the summer of 2001. An additional 16 heliostats were instrumented, for a total of 64 heliostats with over 2300 m^2 of mirror area, filling in the geographical front and center of the heliostat field. The charge-integrating ADCs used by prior versions of STACEE were also removed and replaced with waveform digitizers or "flash ADCs" (FADCs). A brief overview of these improvements follows; additional details are available elsewhere (Scalzo 2004).

2.1. *Optics Upgrades*

Figure 1 shows the NSTTF heliostat field, with the STACEE heliostats indicated. The heliostats are chosen to provide the most uniform ground coverage possible, subject to constraints imposed by the crowding of heliostat images (and PMT apertures) in the focal plane of each secondary mirror. In addition to the three secondaries (1.9 m diameter) used by

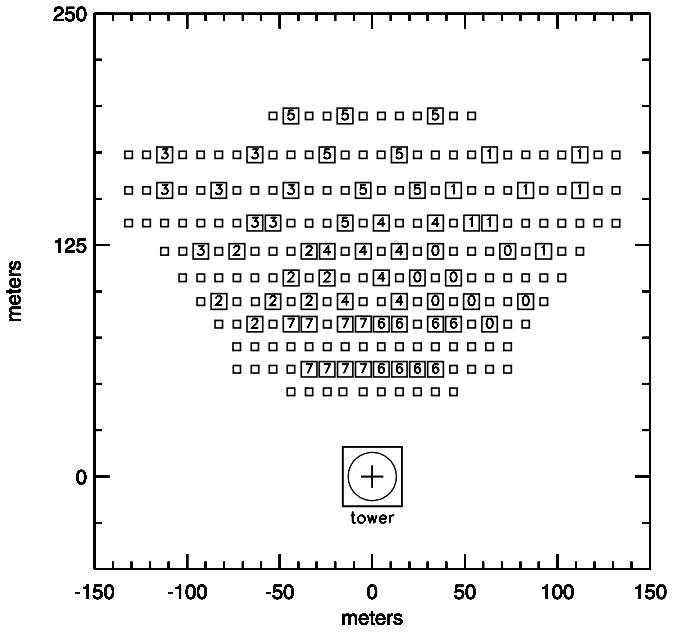

FIG. 1.—Map of the heliostat field used by the STACEE experiment, showing updates to the experiment over time. Heliostats are numbered according to the trigger subcluster to which they belong. Clusters 0, 1, 2, and 3 correspond to the "east" and "west" cameras; most of these heliostats were used in the STACEE-32 prototype. Clusters 4 and 5 correspond to the "north" camera, which was added for STACEE-48. Clusters 6 and 7 correspond to the new STACEE-64 "southeast" and "southwest" cameras. The base of the NSTTF solar tower, which houses the STACEE optics and electronics, marks the origin of the coordinate system.

STACEE-48, two additional secondaries (1.1 m diameter) were built for STACEE-64 to allow the use of additional heliostats at the front of the field. A set of 16 additional camera elements (PMT + DTIRC + housing) were instrumented for the new heliostats. All 64 camera elements were carefully calibrated in the lab and redistributed among the cameras according to measured differences in quantum efficiencies in order to equalize the optical throughput on all detector channels.

Improved understanding of the heliostat optics via Monte Carlo simulations and measurements of the heliostat point-spread function using a CCD camera prompted adjustments to the optical elements. Each STACEE heliostat has 25 mirror facets that can be independently focused and aligned (Hanna et al. 2002); the point-spread function is periodically evaluated and adjustments made, if necessary, using a laser look-back method. Prior to the W Com observing campaign, the facets on many heliostats were readjusted to fix the overall optical axis within the heliostat body frame to a standard position, thereby improving pointing accuracy. The absolute pointing of each heliostat was calibrated to an accuracy of $0^\circ.05$ using drift scans of bright stars.

2.2. *Trigger*

STACEE uses a two-level coincidence trigger described in detail in Martin & Ragan (2000). PMT camera elements are grouped into subclusters of eight PMTs each. The signal from each PMT is AC-coupled, amplified, and discriminated before entering the subcluster trigger electronics. The coincidence trigger accounts for channel-to-channel delays among the discriminated PMT signals, which arise from the geometry of the shower wave front and the differences in propagation times from different parts of the heliostat field; the programmed

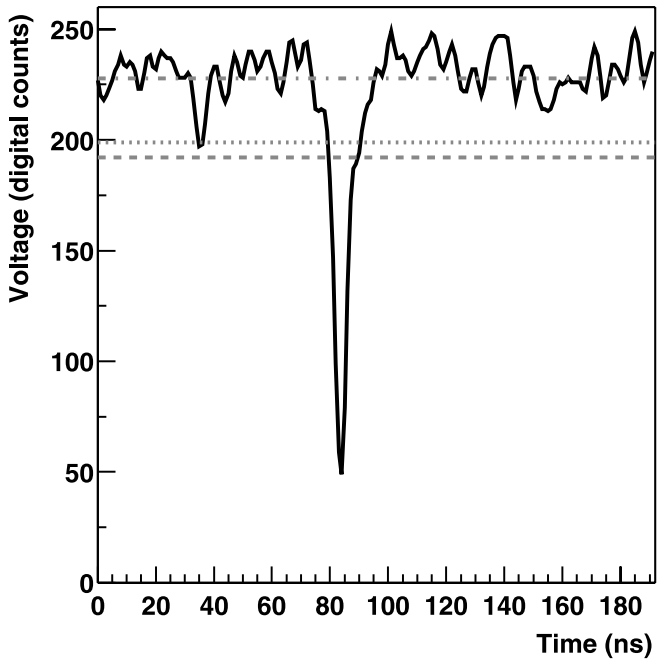

FIG. 2.—Digitized PMT signal from a typical air shower event. *Dot-dashed line*: FADC baseline. *Dashed line*: Discriminator threshold. *Dotted line*: 3 σ above baseline for NSB fluctuations.

delays are accurate to 1 ns. A coincidence test among delayed PMT signals is then made at the subcluster level, and a further coincidence among subclusters is required to trigger event readout. The number of coincident PMTs in a subcluster, and the number of coincident subclusters, are chosen to optimize the quality factor for the rejection of hadronic air showers according to Monte Carlo simulations. The discriminator threshold is then set at a level that makes the overall event trigger rate from chance coincidences of pulses due to fluctuations of NSB photons negligible (less than 0.2 minutes^{-1}).

The STACEE-64 trigger topology is shown in Figure 1. For the W Com observations, the discriminator threshold was set to 140 mV (about 5.5 photoelectrons); five of eight PMTs in a subcluster were required to cross threshold within a narrow coincidence window to generate a subcluster trigger. The precise width of this coincidence window as applied to a given series of pulses varies between 8 and 24 ns because of the implementation of the trigger logic (see Martin & Ragan 2000); the mean width for a two-channel coincidence is 16 ns. Five of eight subcluster triggers within a window of 16 ns were necessary to trigger event readout.

2.3. *FADCs*

The FADCs represent a major upgrade to the STACEE experiment. Access to the full digitized PMT waveform allows not only more accurate measurements of the timing and intensity of the wave front but also measurement of charge-timing correlations, such as the distribution of Cerenkov photon arrival times at each heliostat. Various new methods that use FADC data to reject hadronic events are currently being studied by the STACEE collaboration (Scalzo et al. 2003; Zweerink et al. 2003). The FADCs are also routinely used to calibrate and monitor the gains of the STACEE PMTs using a custom-designed laser calibration system (Hanna & Mukherjee 2001).

The FADCs used by STACEE-64 are a commercial system produced by Acqiris, Inc. The system comes in modular pieces, with four channels per board. Up to six boards (24 channels) fit into a special crate, which runs the Linux operating system. A real-time Linux driver for the system was developed by our group. Each FADC channel samples at 1 GS s^{-1} with a dynamic range of 1 V during normal astronomical observations. A sampled PMT signal from an actual Cerenkov event is shown in Figure 2. The zero points of the FADC inputs are calibrated to a precision of 1 mV rms, and the channel-to-channel gains of the system are equalized to within 0.5%.

In the 2001–2002 observing season, 32 FADC channels were instrumented, each sampling the signal from two PMT channels chosen so that the incoming Cerenkov signals would be well-separated in time. By the 2002–2003 observing season, 64 FADC channels were instrumented so that each FADC sampled the signal from exactly one PMT.

3. OBSERVATIONS AND QUALITY CUTS

STACEE-64 was used to observe W Com in the spring of 2003, from late March to early June. To maximize sensitivity and robustness to systematic effects, STACEE operates in an "ON-OFF" integration mode (Oser et al. 2001). In an ON-OFF observation, each gamma-ray source is assigned another region of the sky at the same declination that contains no known gamma-ray source. The two regions are usually separated by 30 minutes in right ascension. STACEE then tracks the OFF region immediately before or after the ON region, so that the same range of azimuth and elevation are observed, and the detector sensitivity (which depends on azimuth and elevation) is matched in both halves of the pair. Thirty-four ON-OFF pairs were taken on W Com, for a total of 13.5 hr of on-source observing time.

Several quality cuts were then imposed on the data set, as described below. These quality cuts are to be understood as "pairwise time cuts," in the sense that if data in a certain time interval during one run are flagged and removed from the data set, then data in the corresponding time interval in the other run of the pair (i.e., spanning the same local horizon coordinates) are also removed.

The control system for the NSTTF heliostats continually records status information that can be used to pinpoint malfunctions on particular heliostats. This status information is logged nightly and merged with the regular STACEE data product. Portions of runs during which any heliostat malfunctioned were flagged and removed from the data set.

As observed in Boone et al. (2002), the subcluster trigger rates are very sensitive to fluctuations in sky conditions, since they vary as a high power of the discriminator rates on PMTs within the cluster, which in turn are dominated by fluctuations of NSB photons. Large deviations of the subcluster trigger rates from a smooth linear trend have been seen to correlate strongly with unstable weather conditions. After heliostat cuts, an iterative procedure was used to identify and flag affected portions of the data. Each pair was divided into 30 s time bins, and a least-squares fit to the time-averaged subcluster rates performed repeatedly, excluding outliers beyond a certain tolerance at each iteration. In order for a bin to merit exclusion from the data set, deviations in the rates had to appear for at least four of eight subclusters. After undergoing this process, if a pair of data had less than 1 minute of data remaining, this pair was simply excluded from further analysis.

In addition, some data were removed because of malfunctions in the data acquisition program resulting in the loss or corruption of FADC data, which is needed for the final

TABLE 1
RESULTS OF FIELD BRIGHTNESS CORRECTIONS

Source	t_{ON}[a] (s)	t_{OFF}[a] (s)	N_{ON}	N_{OFF}	Significance (σ)[b]
Quality Cuts Only					
ι CrB	11,777.4	12,064.9	75,505	73,060	+10.99
21 Com	6053.2	6148.7	32,354	31,299	+6.16
HIP 89729	19,087.2	19,191.8	74,823	73,292	+5.03
W Com	37,767.0	37,955.5	219,031	217,085	+4.60
Library Padding					
ι CrB	11,777.4	12,064.9	52,423	53,367	+1.02
21 Com	6053.2	6148.7	22,859	23,269	−0.23
HIP 89729	19,087.2	19,191.8	53,463	53,678	+0.24
W Com	37,767.0	37,955.5	155,722	156,006	+0.88
Dynamic Thresholds					
ι CrB	11,234.1	11,508.5	58,566	60,556	−1.60
21 Com	5522.8	5613.9	25,172	25,305	+1.25
HIP 89729	18,731.9	18,835.3	61,990	62,064	+0.76
W Com	36,982.9	37,168.9	182,433	182,942	+0.67

NOTES.—Results of field brightness corrections for three stars of varying magnitude and for W Com. The live times and raw excesses of events in the ON and OFF runs, and the corresponding significance, are shown for each technique.

[a] Integrated live time after quality cuts and dead-time correction. Note that these represent equal amounts of actual observing time in the ON and OFF runs, but that differences in the trigger rate may lead to differences in the detector dead time between the ON and OFF runs.

[b] Significance in standard deviations (σ). Calculated according to Li & Ma (1983).

analysis (see below). About 2% of the original data set was removed for this reason.

Finally, even though the pairwise time cuts equalize the observing times in the on-source and off-source data sets, a live-time correction is necessary. The time required for the data acquisition software to read out each triggered event creates dead time within the observing intervals, which is rate-dependent and measured electronically by the detector as the data are acquired.

After all quality cuts, a total of 10.5 hr of on-source observing time remained, distributed among 32 ON-OFF pairs (see Table 1). Using the Li & Ma (1983) expression for the significance gives a (raw) positive significance of 4.6 σ, at a live-time–corrected excess event rate of 4.8 ± 1.1 minutes^{-1}.

4. SKY BRIGHTNESS CORRECTIONS

Before deriving an integral flux or upper limit, it is very important to correct the raw trigger rate for any differences in NSB fluctuations between the on-source and off-source fields. NSB photons entering the detector frequently promote sub-threshold hadronic air showers above the detection threshold, even under the best conditions. The promotion rate increases as the sky brightness increases so that if the on-source field is slightly brighter than the off-source field, either because of stars or to subtle variations in atmospheric conditions, the resulting excess in the *hadronic* trigger rate can mimic a gamma-ray excess. Similarly, if the off-source field is brighter than the on-source field, an existing gamma-ray excess may be masked; a net deficit may even appear. An accurate measurement of the true gamma-ray rate therefore requires a correction for the promotion effect.

We have developed three independent methods to correct for the effects of varying levels of NSB light on the co-incidence trigger. We find that the excess we see from W Com is consistent with the promotion of events representing only hadronic showers, with no additional gamma-ray component.

4.1. *Direct Measurement of the Hadronic Promotion Trend*

One method of correcting for field brightness effects was demonstrated by the analysis of the STACEE-48 observations of Mrk 421 (Boone et al. 2002). The excess brightness in the STACEE on-source field for Mrk 421 was due mainly to a single bright star, HD 95934 (6.16 mag in the *B* band). No FADC data were available at that time, but the promotion rate was estimated simply by taking ON-OFF pairs on another star, HIP 80460, with a similar *B*-band magnitude. The measured promotion rate was then subtracted from the total excess to give the gamma-ray excess.

Similar observations have been made for STACEE-64 and are depicted in Figure 3. Three stars of different magnitudes and suitable declinations (21 Com, ι CrB, and HIP 89279) were selected and observed as if they were gamma-ray sources. The excess rate is plotted as a function of a weighted average current difference,

$$\Delta I = \frac{\sum_{j=1}^{64} \langle w_j \Delta I_j \rangle}{\sum_{j=1}^{64} \langle w_j \rangle}, \quad (1)$$

where ΔI_j is the ON-OFF difference in anode current on PMT j, w_j is the measured fraction of triggered events in which PMT j crossed threshold, and the angle brackets denote time averaging over the entire data set. The promotion trend is well-fitted ($\chi^2/\mathrm{dof} = 1.04$) by a straight line with slope 3.7 ± 0.3 minutes^{-1} μA^{-1}; it represents a zero-signal baseline for gamma-ray sources observed by STACEE.

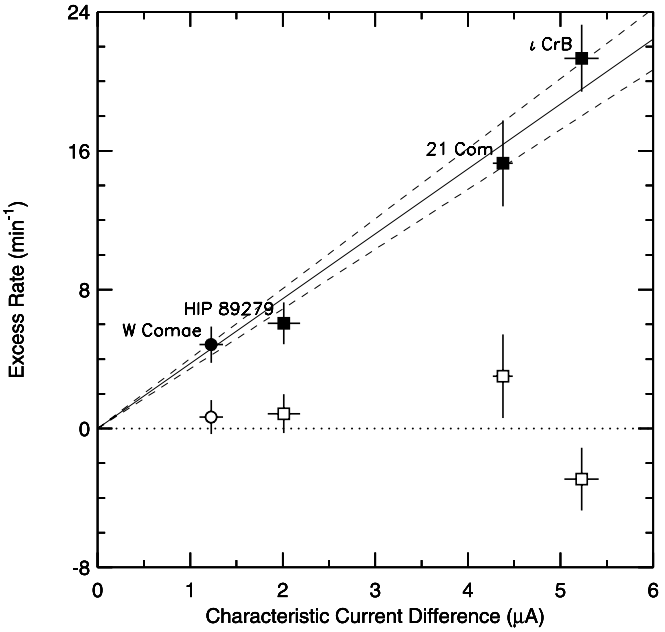

FIG. 3.—Excess event trigger rates as a function of the characteristic current difference for sources observed in 2002–2003 by STACEE-64. *Squares*: Star observations. *Circles*: W Com. *Filled symbols*: Raw excess. *Open symbols*: Excess after the dynamic threshold brightness correction. The lines show the best-fit linear trend constrained to go through the origin (*solid line*) with 68% confidence errors on the slope (*dashed line*), and the zero-rate baseline (*dotted line*).

The raw rate measurement for W Com is also shown on the plot, and it is consistent with the promotion trend. Subtracting the expected number of promotion events from the W Com excess based on its characteristic current leaves a net excess of 0.2 ± 1.2 minutes^{-1}.

The direct measurement of the promotion trend is intuitive and straightforward and can be used to quickly assess how much of an observed excess is due to promotion. However, the promotion trend as measured reflects the observing season on average, and in particular observing conditions during the star runs, rather than conditions that might pertain for individual runs in the data set for a particular gamma-ray source. An event-by-event, channel-by-channel treatment is therefore more desirable when deriving scientific results such as fluxes or upper limits. A sizable data set of star observations proved quite valuable for testing such brightness correction techniques.

4.2. *Software Padding Using Waveform Libraries*

Another technique, commonly referred to as "padding," has been in use in some form by atmospheric Cerenkov telescopes since their inception. For example, in the early days of the Whipple 10 m imaging telescope, NSB conditions were equalized in hardware by using a small LED on the face of each PMT in a feedback loop (Weekes et al. 1989). Later, the equalization was done in software by adding random Gaussian deviates to the recorded ADC values to mimic fluctuations from increased NSB levels (Cawley 1993) and then reimposing an additional selection criterion similar to the hardware trigger. For STACEE, the trigger depends not only on charge distributions but also on relative timing, since the light from an air shower reaches different parts of the detector at different times. Knowledge of the PMT waveforms as provided by the FADCs is therefore necessary to do software padding.

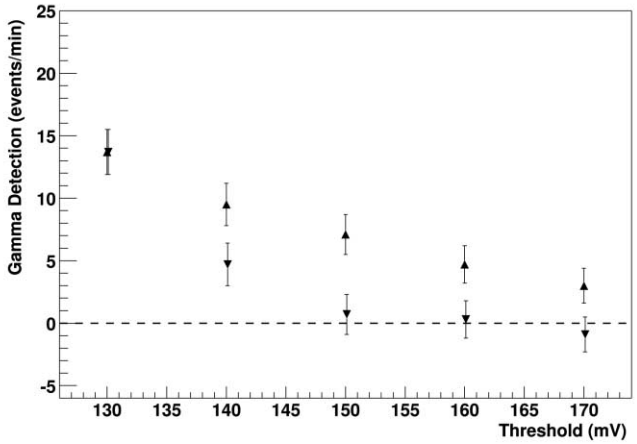

FIG. 4.—Excess event trigger rate as a function of FADC analysis threshold in the library padding analysis of a subset of data taken on the star ι CrB. The trigger condition is described in the text. *Upright triangles*: No padding of traces before retriggering. *Inverted triangles*: Traces are padded to equalize rms before retriggering. *Dashed line*: Zero promotion excess. The figure shows that the minimum threshold necessary to remove all hadronic promotion events from the library-padded data set is 150 mV.

A software padding scheme has been implemented and tested by STACEE as follows. FADC waveforms corresponding to varying NSB levels were sampled from 16 of the PMTs in situ under controlled conditions. The waveforms were characterized by their rms fluctuations and stored in a library to be used in padding. In the padding analysis, these library waveforms were added to the waveforms in the observation data set to equalize the rms fluctuations in both runs of a pair, as measured by the 400 ns section of the waveform immediately preceding the event trigger. An off-line reimposition of the trigger required five of eight PMTs in a subcluster, and five of eight subclusters, to fire within a coincidence window of width 16 ns.

When reimposing the trigger in software, the analysis threshold at which the FADC waveforms are discriminated must be increased over the nominal hardware discrimination threshold. Adding background noise to waveforms from recorded events in a low-noise run equalizes only the probability that an event will pass additional off-line cuts relative to an event in the corresponding high-noise run. It is impossible to recover events that *would* have appeared in the low-noise data set if the additional noise had been physically present at the outset. A subset of the ON-OFF data for ι CrB was used to optimize the off-line analysis threshold (see Fig. 4). The analysis threshold was set to 150 mV for all FADC channels based on the results of this optimization.

The results of the library padding brightness correction procedure are shown in Table 1. For all three stars and for W Com, the ON-OFF difference drops from a significant excess in the uncorrected data to an insignificant difference in the corrected data. In particular, the significance drops from 4.6 to 0.9 σ for W Com.

4.3. *Dynamic Thresholds*

Although software padding has clearly been successful in eliminating the promotion excess, it has the drawback that the software discriminator threshold used to analyze FADC waveforms, and hence the energy threshold for the analysis, must be raised significantly. The desire to maintain a low discriminator threshold in the off-line analysis of FADC data

formed the motivation for investigating what we call the "dynamic thresholds" technique.

In the absence of NSB fluctuations, the distribution of pulse heights for pulses within the trigger coincidence window on each channel would depend only on the intensity of Cerenkov light from air showers. The presence of NSB fluctuations on a channel has two effects on the pulse-height spectrum. First, the linear superposition of fluctuating background traces on the underlying pulses from Cerenkov photons produces an additional statistical uncertainty in the pulse-height measurement for each event by changing the pedestal from which the pulse height is measured. NSB fluctuations therefore smear out the underlying air shower pulse-height distribution. Second, NSB fluctuations occasionally cross the discriminator threshold within the coincidence window even when no signal pulse is present, resulting in a second component to the pulse-height distribution.

The dynamic thresholds technique models both of these effects quantitatively to predict changes in the analysis thresholds. When comparing the on-source and off-source runs of a pair, the run with larger fluctuations in the baseline trace will have a higher promotion rate and therefore a lower effective discriminator threshold. To compensate for promotion, for each channel the threshold in the noisier run is raised so that the rate of *background* pulses (NSB + hadronic Cerenkov light) within the coincidence window, and with pulse height above the analysis threshold, is the same in both halves of the pair. When a coincidence condition among pulses is imposed off-line, this prescription should remove a number of events equal to the expected number of promoted hadronic shower events, while retaining sensitivity to any possible gamma-ray excess.

For the off-source run, only hadronic air showers and NSB photons contribute to the pulse-height distribution, so that the rate of pulses above the analysis threshold can be directly measured. The pulse-height distribution for the on-source run, however, may also contain Cerenkov pulses from gamma-ray air showers. Thus, the form of the on-source pulse-height spectrum *without* the gamma-ray contribution must be predicted from the measured off-source pulse-height spectrum and measurements of the NSB fluctuations.

We used a semianalytic approach to predict the form of the on-source pulse-height spectrum (for details, see Scalzo 2004). Histograms of individual waveform samples were accumulated using the part of each waveform immediately preceding the event trigger. These histograms characterized the distribution of fluctuations, denoted $s_{\rm ON}(V)$ and $s_{\rm OFF}(V)$, in the waveform baseline (and hence in the effective discriminator threshold) due to NSB fluctuations in each run. The pulse-height distribution for all pulses within the coincidence trigger window for the off-source run, denoted $R_{\rm OFF}(V)$, was also measured. We predicted the form of the on-source pulse-height spectrum $R_{\rm ON}(V)$ as follows.

1. Fit $s_{\rm OFF}(V)$, $s_{\rm ON}(V)$, and $R_{\rm OFF}(V)$ with smooth analytic forms to interpolate between thresholds.

2. Normalize $s_{\rm OFF}(V)$ with respect to $R_{\rm OFF}(V)$ using the measured off-source PMT rate (which is dominated by NSB fluctuations) and subtract it from $R_{\rm OFF}(V)$ to obtain a pulse-height spectrum representing only pulses due to hadronic air showers.

3. Deconvolve this hadronic pulse-height spectrum by $s_{\rm OFF}(V)$ to obtain $R_0(V)$, the expected hadronic air shower pulse-height spectrum in the absence of NSB fluctuations.

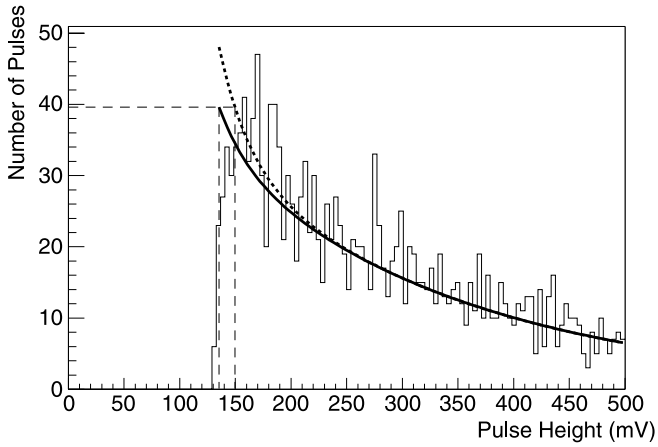

FIG. 5.—Pulse-height distribution of triggered events from a 10 minute segment of a typical off-source run on the star ι CrB. The best-fit form of a Poisson distribution (expected NSB) plus an exponential is shown (*solid line*), as well as the predicted form for the on-source run (*dashed line*) resulting from additional NSB fluctuations. The on-source prediction is normalized to the same detector live time as the off-source best fit. *Horizontal dashed line*: Number of off-source pulses per mV at the nominal hardware discriminator threshold. *Vertical dashed lines*: Analysis thresholds ON and OFF necessary to equalize the number of pulses above threshold over the course of the run.

4. Convolve $R_0(V)$ by $s_{\rm ON}(V)$ to account for the NSB fluctuations in the on-source run.

5. Normalize $s_{\rm ON}(V)$ using the measured PMT rate on-source and add it to the convolution of $R_0(V)$ and $s_{\rm ON}(V)$ to obtain the predicted form of $R_{\rm ON}(V)$.

Figure 5 shows an example of the results of this procedure for one STACEE channel in the data set for the star ι CrB. A visual inspection of Figure 5 indicates that the threshold on this channel must be increased by 15 mV. This figure represents the worst-case scenario, corresponding to conditions on one of the noisiest channels during observations of the brightest of the three padding stars. For the W Com observations, the mean increase in the software discriminator threshold is approximately 2 mV, considerably smaller than the 10 mV adjustment on *all* channels necessary for software padding.

The dynamic thresholds for a run were always calculated after quality cuts to eliminate systematics due to rapidly fluctuating sky conditions. To improve robustness against slow drifts in sky conditions, each 28 minute run was partitioned into three equal segments 560 s in length. The statistics within each segment were sufficient to establish the form of the sampled distributions, except in cases in which time cuts had already removed most of the segment. If statistics within a segment did not permit a reliable prediction of the threshold adjustments, the segment and its counterpart in the other half of the pair were removed from the data set. Less than 3% of the quality-cut data set was removed in this way; the remaining data set comprised 10.3 hr of on-source observing.

The results of the dynamic threshold analysis for W Com, and for the three stars observed by STACEE for promotion studies, are shown in Table 1. As with library padding, no statistically significant excess remains on any of the stars, or on W Com, after the dynamic threshold technique is applied to the raw data sets.

5. FLUX LIMIT DETERMINATION

To calculate an upper limit on the flux of gamma rays from W Com, two main ingredients are necessary: an assumption

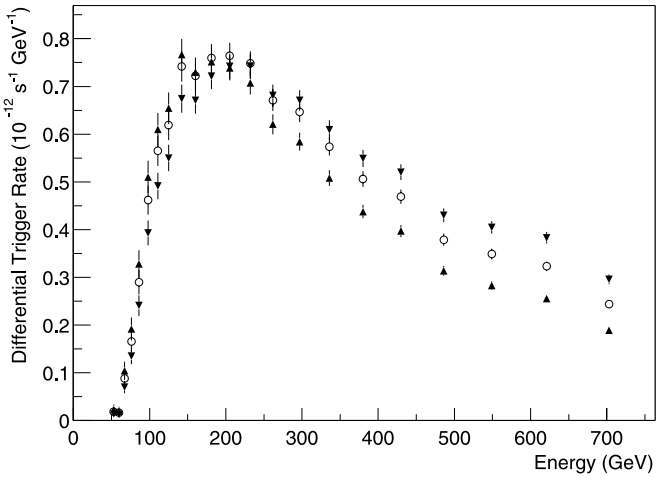

FIG. 6.—STACEE-64 simulated trigger rate vs. energy for a power-law differential flux spectrum of gamma rays with photon index $\alpha = 1.55$ (*inverted triangles*), $\alpha = 1.73$ (*circles*), and $\alpha = 1.91$ (*triangles*). All spectra are normalized to the same integral flux above 50 GeV.

about the shape of the spectrum, and knowledge of the detector response. The latter was produced from Monte Carlo simulations. We use the CORSIKA simulation package (Heck et al. 1999) to simulate air showers, using the QGSJET model (Kalmykov et al. 1997) for hadronic interactions at energies above 100 GeV. The detector was modeled using software written by the collaboration, including a full ray trace of the detector optics and detailed simulations of the discriminators, the delay and trigger systems, and the FADCs. The full simulation chain successfully reproduces important detector-related quantities, such as the discriminator rate on each PMT, the trigger rate of cosmic-ray air shower triggers at zenith, and the increase in the hadronic trigger rate resulting from NSB fluctuations.

The response of the STACEE detector is characterized by the effective area, defined as a function of energy by

$$A(E) = \int_G P(x,\ y,\ E)\, dx\, dy, \qquad (2)$$

where $P(x, y, E)$ is the probability that a gamma-ray air shower with shower core landing at position (x, y) produces an event trigger and G is a region on the ground [the (x, y)-plane] containing all (x, y) for which $P(x, y, E) \neq 0$. The functional form of the effective area used to obtain the integral flux limits in this paper is an average of the results of simulations done in different regions of the sky, at a declination of $+28^{\circ}.23$ spaced in 10° increments in hour angle, each weighted by its exposure in the 2003 data set. The sensitivity to very low energy air showers is highest for a source at transit. However, about 80% of the 2003 W Com data were taken between hour angles of $+20^{\circ}$ and $+40^{\circ}$ (zenith angles between 10° and 26°). The large zenith angles result in a loss of sensitivity for low-energy air showers with respect to that expected for the source at transit. First, the Cerenkov photon density of the shower decreases, and the area of the Cerenkov light pool increases, with increasing zenith angle. Second, off-axis aberrations in the heliostat optics broaden the heliostat point-spread function for sky locations far from transit, decreasing the overall optical throughput.

The effective area must also account for any energy dependence introduced by the off-line trigger cut used in the analysis. Of the three analysis methods available to correct for field brightness differences, the dynamic threshold technique maintains the best sensitivity at low energies, and we use this technique to establish our upper limit.

In previous STACEE publications (Oser et al. 2001; Boone et al. 2002), the energy threshold has been quoted as the energy at which the differential gamma-ray trigger rate (effective area × expected photon flux from the assumed model) reaches a maximum. We continue to do so in this paper, quoting an energy threshold for each assumed model accordingly. We assume that the errors in the absolute throughput calibration of the independent elements (heliostat optics, PMT quantum efficiency, etc.) of the STACEE detector are Gaussian and uncorrelated. These errors may then be added in quadrature to obtain the systematic uncertainty in the absolute energy scale calibration, which we estimate to be 20%. The systematic errors on the energy threshold are determined by rescaling the energy scale at which the effective area is evaluated by ±20%

TABLE 2
INTEGRAL FLUX UPPER LIMITS FOR POWER-LAW SPECTRA

Emission Model	$\tau_{\gamma\gamma}$[a]	$E_{\rm thresh}$[b] (GeV)	95% CL[c] (10^{-10} cm^{-2} s^{-1})	$\Phi(> E_{\rm thresh})$[d] (10^{-10} cm^{-2} s^{-1})
$\alpha = 1.55$	low	191^{+44}_{-30}	0.48	7.28
$\alpha = 1.55$	high	186^{+22}_{-29}	0.52	3.87
$\alpha = 1.73$	low	186^{+31}_{-30}	0.49	2.23
$\alpha = 1.73$	high	170^{+26}_{-16}	0.60	1.49
$\alpha = 1.91$	low	168^{+38}_{-26}	0.56	0.73
$\alpha = 1.91$	high	160^{+20}_{-23}	0.65	0.52

NOTES.—Upper limits on the integral flux of gamma rays from W Com, assuming that the differential flux of photons follows a power law [$\Phi(E) \propto E^{-\alpha}$]. Power laws were extrapolated from the Third EGRET Catalog (Hartman et al. 1999) and corrected for EBL absorption. The mean spectral index $\alpha = 1.73$ is used, as well as low and high values consistent with the errors on the power-law fit to the EGRET data.

[a] Optical depth to pair production $\gamma\gamma \longrightarrow e^+e^-$ against the EBL from a redshift of $z = 0.102$ (from Aharonian 2001). The extreme low and high predictions for $\tau_{\gamma\gamma}$ were used in this table.

[b] STACEE energy threshold for the assumed model. The energy threshold is defined as the energy at which the differential trigger rate (effective area × gamma-ray flux) reaches a maximum. Systematic errors as shown represent propagation of the error in the calibration of the absolute energy scale using the mean effective area curve.

[c] STACEE 95% confidence level upper limit on the integral flux above the energy threshold.

[d] Expected flux above the energy threshold according to the emission model.

TABLE 3

INTEGRAL FLUX UPPER LIMITS FOR LEPTONIC MODELS

Emission Model	$E_{\rm thresh}$[a] (GeV)	95% CL[b] (10^{-10} cm^{-2} s^{-1})	$\Phi(>E_{\rm thresh})$[c] (10^{-10} cm^{-2} s^{-1})
SSC fit 1	...	1.35	0.0278
SSC fit 2	112^{+26}_{-18}	1.39	0.0603
SSC fit 3	108^{+26}_{-18}	1.55	0.0876
SSC fit 4	97^{+24}_{-13}	2.12	0.139
SSC fit 5	86^{+15}_{-8}	3.49	0.17
SSC fit 6	95^{+23}_{-12}	2.36	0.0276
SSC fit 7	100^{+25}_{-15}	1.94	0.331
SSC+EC fit 8	112^{+26}_{-18}	1.37	0.0303
SSC+EC fit 9	110^{+26}_{-18}	1.41	0.0344
SSC+EC fit 10	108^{+27}_{-18}	1.44	0.0467

NOTES.—Upper limits on the integral flux of gamma rays from W Com, according to various leptonic (SSC, SSC+EC) models of the relativistic jet described in Boettcher et al. (2002). Because of the sharp cutoff in the expected gamma-ray emission spectra above $\sim$100 GeV, EBL absorption should be negligible for the leptonic models.

[a] STACEE energy threshold for the assumed model. The energy threshold is defined as the energy at which the differential trigger rate (effective area $\times$ gamma-ray flux) reaches a maximum. Systematic errors as shown represent propagation of the error in the calibration of the absolute energy scale using the mean effective area curve.

[b] STACEE 95% confidence level upper limit on the integral flux above the energy threshold.

[c] Expected flux above the energy threshold according to the emission model.

and calculating the resulting shift in the maximum of the differential gamma-ray trigger rate.

Figure 6 demonstrates the calculation of the energy threshold for an extrapolation of the EGRET power-law spectrum for W Com ($\alpha = 1.73 \pm 0.18$), using the exposure-averaged effective area. Curves representing the low and high values for the spectral index within the EGRET experimental errors ($\alpha = 1.55$ or 1.91) are also shown, normalized to the same integral flux above 50 GeV. At transit, at a zenith angle of $6^\circ.73$, the energy threshold is about 120 GeV for $\alpha = 1.73$. The energy threshold using the exposure-averaged effective area curve is 170 GeV. For the $\alpha = 1.73$ model, therefore, we quote our result at an energy threshold of 170 ± 40 GeV. This threshold changes by about 20 GeV if the low or high value of α (1.55 or 1.91) is used instead.

Tables 2, 3, and 4 show upper limits from STACEE observations for selected models of the gamma-ray emission from W Com (Boettcher et al. 2002). In each case, the optical depth for pair production against the EBL has been taken into account. The models are based on the semianalytic approaches of Primack et al. (1999, 2001), which use a top-down, hierarchical treatment of structure formation as tuned to fit recent EBL measurements. The qualifiers "low" and "high" refer to the extreme low (LCDM-Salpeter; Primack et al. 1999) and high (Kennicutt; Primack et al. 2001) predictions for the optical depth to pair production at $z = 0.102$ from

TABLE 4

INTEGRAL FLUX UPPER LIMITS FOR HADRONIC MODELS

Emission Model	$\tau_{\gamma\gamma}$[a]	$E_{\rm thresh}$[b] (GeV)	95% CL[c] (10^{-10} cm^{-2} s^{-1})	$\Phi(>E_{\rm thresh})$[d] (10^{-10} cm^{-2} s^{-1})
SPB fit 1	low	127^{+22}_{-19}	0.93	0.87
SPB fit 1	high	126^{+16}_{-18}	1.05	0.66
SPB fit 2	low	150^{+14}_{-16}	0.72	2.48
SPB fit 2	high	146^{+14}_{-16}	0.77	1.91
SPB fit 3	low	164^{+29}_{-28}	0.58	0.40
SPB fit 3	high	157^{+22}_{-26}	0.67	0.26
SPB fit 4	low	163^{+30}_{-27}	0.59	0.44
SPB fit 4	high	156^{+22}_{-26}	0.69	0.30
SPB fit 5	low	160^{+40}_{-28}	0.60	0.46
SPB fit 5	high	141^{+36}_{-23}	0.82	0.36

NOTES.—Upper limits on the integral flux of gamma rays from W Com, according to various hadronic (SPB) models of the relativistic jet described in Boettcher et al. (2002).

[a] Optical depth to pair production $\gamma\gamma \longrightarrow e^+e^-$ against the EBL from a redshift of $z = 0.102$ (from Aharonian 2001). The extreme low and high predictions for $\tau_{\gamma\gamma}$ were used in this table.

[b] STACEE energy threshold in for the assumed model. The energy threshold is defined as the energy at which the differential trigger rate (effective area $\times$ gamma-ray flux) reaches a maximum. Systematic errors as shown represent propagation of the error in the calibration of the absolute energy scale using the mean effective area curve.

[c] STACEE 95% confidence level upper limit on the integral flux above the energy threshold.

[d] Expected flux above the energy threshold according to the emission model.

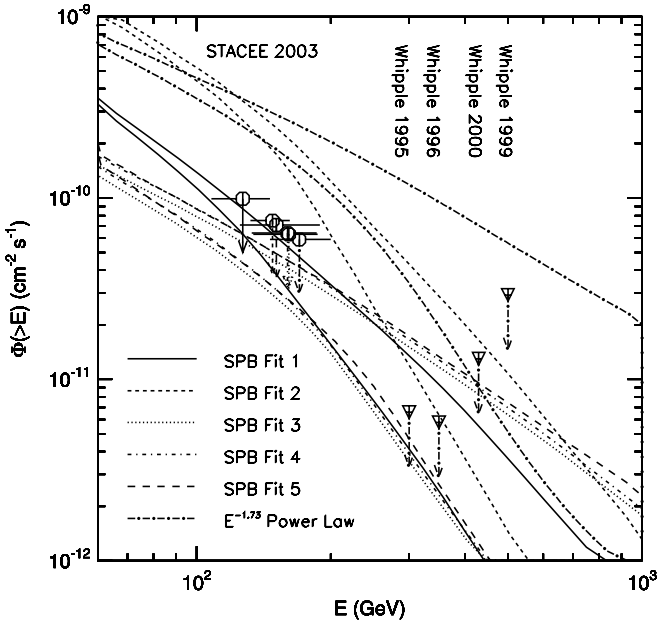

FIG. 7.—Integral flux in cm^{-2} s^{-1} for each of the five SPB models from Boettcher et al. (2002), and for the extrapolation of the best-fit EGRET power law (Hartman et al. 1999). Model predictions for both low and high EBL optical depth are shown, along with STACEE upper limits for mean EBL optical depth. Upper limits from observations with the Whipple 10 m from 1995 to 2000 are also shown (Horan et al. 2003).

specific instances of these semianalytic models, as detailed in Aharonian (2001) and Boettcher et al. (2002).

It is apparent that even when EBL absorption is taken into account, the STACEE results place strong constraints on the extrapolation of the EGRET power law to higher energies. A steeper value of the spectral index, within the uncertainties, is favored. As noted by Boettcher et al. (2002), however, the EGRET data were not taken simultaneously with the measurements at other wavelengths. The possible power-law spectrum may therefore represent a transient flaring state. Moreover, the EGRET power law is fitted to a co-addition of many low significance ($\sim 2\ \sigma$) detections from different epochs, with large uncertainties on the flux and spectral index. In fact, the leptonic model fits shown used only the *BeppoSAX* X-ray data, which is of higher quality; no pure SSC model can fit both the X-ray and EGRET data simultaneously.

The STACEE observations are unable to place interesting constraints on most of the leptonic models, with the expected fluxes being an order of magnitude or more below the STACEE limit in each case. The low predicted fluxes may be anticipated from the sharp spectral cutoff in each model at or below 100 GeV, because of a similar sharp cutoff in the electron energy spectrum at $\gamma_{e,\max} \sim 5 \times 10^4$. Since the dominating factor is the availability of energy in relativistic electrons, the cutoff energy in the modeled gamma-ray spectra is approximately independent of the density of external target photons in SSC+EC models. The cutoff in the electron energy spectrum is constrained tightly by the X-ray data, which lie between the falling edge of the low-energy (electron synchrotron) peak in the spectrum and the high-energy peak.

On the other hand, most of the hadronic models predict integral fluxes above the energy threshold that are only slightly below the corresponding upper limits from the STACEE observations. In particular, we can exclude SPB model 2 at 95% confidence. Among all the hadronic models shown, model 2 has the highest cutoff for the proton energy distribution ($\gamma_{p,\max} = 3 \times 10^9$), yet the magnetic field, the Doppler factor of the jet, etc., are comparable to the other models.

Figure 7 shows the STACEE upper limits for the hadronic models in a graphic form. The figure shows that STACEE is quite close to the sensitivity necessary to begin to distinguish between the various hadronic models for W Com. However, the constraints provided by precise, simultaneous observations at other wavelengths are necessary, in addition to STACEE observations, because of the potential high-energy variability of blazars such as W Com. The constraints placed by the X-ray observations from *BeppoSAX* were instrumental in shaping the predictions for the gamma-ray spectra for the hadronic models presented here. Figure 7 also shows upper limits from high-energy observations made using the Whipple 10 m imaging Cerenkov telescope (Horan et al. 2003) from 1995 to 2000. (The energy thresholds for the Whipple limits were each calculated assuming a power law with spectral index $\alpha = 2.5$ and do not yet address specific emission models.) Each instrument operates within a different regime of sensitivity and energy, and the scientific payoff for a variable target is maximized when observations are made simultaneously. Further STACEE observations in the future, coupled with new off-line hadronic rejection techniques to improve the flux sensitivity, should allow STACEE to further explore the parameter space for the hadronic models, especially when contributing to a multi-wavelength monitoring campaign.

6. CONCLUSIONS

The STACEE-64 observations in the spring of 2003 were made at a lower energy threshold than any other atmospheric Cerenkov telescope has yet attained for W Com. STACEE detects no significant emission from W Com, resulting in 95% CL upper limits on the integral flux above this threshold in various hadronic emission models at the level of 10^{-10} cm^{-2} s^{-1}. While leptonic models predict a flux that falls below this level, extrapolations of the best-fit EGRET power law, and some synchrotron-proton hadronic models, predict an integral gamma-ray flux above the energy threshold close to or exceeding the upper limit from STACEE observations. Additional STACEE observations planned for the spring of 2004 ought to either exclude these models at a significantly higher confidence level, or detect gamma-ray emission from W Com if these models provide an adequate description of the source.

We are grateful to the staff at the National Solar Thermal Test Facility, who continue to support our science with enthusiasm and professionalism. Thanks to Markus Boettcher and Anita Reimer for providing gamma-ray spectra predicted by their leptonic and hadronic emission models of W Com. Thanks also to Teresa Spreitzer, Audry Alabiso, Joshua Boehm, Nathan Kundtz, Dan Schuette, and Claude Théoret. This work was supported in part by the National Science Foundation, the Natural Science and Engineering Research Council of Canada (NSERC), Fonds Québécois de la Recherche sur la Nature et les Technologies (FQRNT), the Research Corporation, and the California Space Institute.

REFERENCES

Aharonian, F. A. 2000, NewA, 5, 377
———. 2001, Proc. 27th Int. Cosmic-Ray Conf. (Hamburg, Germany), 250
Bloom, S. D., & Marscher, A. P. 1996, ApJ, 461, 657
Boettcher, M., Mukherjee, R., & Reimer, A. 2002, ApJ, 581, 143
Boone, L. M., et al. 2002, ApJ, 579, L5
Cawley, M. 1993, in Towards a Major Atmospheric Cerenkov Detector II, for TeV Astro/particle Physics, ed. R. C. Lamb (Ames: Iowa State Univ. Press), 176
Coppi, P. S., & Aharonian, F. A. 1999, ApJ, 521, L33
de Naurois, M., et al. 2002, ApJ, 566, 343
Dermer, C. D., Schlickeiser, R., & Mastichiadis, A. 1992, A&A, 256, L27
Hanna, D. S., & Mukherjee, R. 2001, Nucl. Instrum. Methods A, 482, 271
Hanna, D. S., et al. 2002, Nucl. Instrum. Methods A, 491, 126
Hartman, R. C., et al. 1999, ApJS, 123, 79
Heck, D., Knapp, J., Capdevielle, J. N., Schatz, G., & Thou, T. 1999, Rep. FZKA 6019, Forschungszentrum Karlsruhe
Horan, D., et al. 2003, Proc. 28th Int. Cosmic-Ray Conf. (Tsukuba, Japan), 2567
Kalmykov, N. N., et al. 1997, Nucl. Phys. B (Proc. Suppl.), 52B, 113
Konopelko, A., et al. 2003, Proc. 28th Int. Cosmic-Ray Conf. (Tsukuba, Japan), 2611
Li, T. P., & Ma, Y. Q. 1983, ApJ, 272, 317
Malkan, M., & Stecker, F. 2001, ApJ, 555, 641
Mannheim, K. 1993, A&A, 269, 67
———. 1995, Astropart. Phys., 3, 295
Martin, J.-P., & Ragan, K. 2000, Proc. IEEE, 12, 141
Mücke, A., & Protheroe, R. J. 2000, in AIP Conf. Proc. 515, Towards a Major Atmospheric Cerenkov Detector VI, ed. B. L. Dingus, M. H. Salamon, & D. B. Kieda (Melville: AIP), 149
Mücke, A., et al. 2003, Astropart. Phys., 18, 593
Ning, X., Winston, R., & O'Gallagher, J. 1987, Appl. Opt., 26, 300
Oser, S., et al. 2001, ApJ, 547, 949
Primack, J. R., Bullock, J. S., Somerville, R. S., & MacMinn, D. 1999, Astropart. Phys., 11, 93
Primack, J. R., et al. 2001, in AIP Conf. Ser. 558, High-Energy Gamma-Ray Astronomy, ed. F. Aharonian & H. J. Völk (Melville: AIP), 463
Scalzo, R. A. 2004, Ph.D. thesis, Univ. Chicago
Scalzo, R. A., et al. 2003, Proc. 28th Int. Cosmic-Ray Conf. (Tsukuba, Japan), 2799
Sikora, M., Begelman, M. C., & Rees, M. J. 1994, ApJ, 421, 153
Tagliaferri, G., et al. 2000, A&A, 354, 431
Théoret, C. G. 2001, Ph.D. thesis, McGill Univ.
Tripathi, S. M., et al. 2002, BAAS, 34, 676
Urry, C. M., & Padovani, P. 1995, PASP, 107, 715
Weekes, T. C. 1988, Phys. Rep., 160, 1
Weekes, T. C., et al. 1989, ApJ, 342, 379
Zweerink, J. A., et al. 2003, Proc. 28th Int. Cosmic-Ray Conf. (Tsukuba, Japan), 2795